A platform of patient-derived microtumors identifies individual treatment responses and therapeutic vulnerabilities in ovarian cancer.

Nicole Anderle[1]*, André Koch[2], Berthold Gierke[3], Anna-Lena Keller[1], Annette Staebler[4], Andreas Hartkopf[2], Sara Y. Brucker[2,5], Michael Pawlak[3], Katja Schenke-Layland[1,2,5,6,7], Christian Schmees[1]*

[1]NMI Natural and Medical Sciences Institute at the University of Tuebingen, Reutlingen, 72770 Germany.

[2]Department of Women's Health, Eberhard Karls University Tuebingen, Tuebingen, 72076 Germany.

[3]NMI Technologie Transfer GmbH, Pharmaservices Protein Profiling, Reutlingen, 72770 Germany.

[4]Institute of Pathology and Neuropathology, Eberhard Karls University Tuebingen, Tuebingen, 72076 Germany.

[5]Cluster of Excellence iFIT (EXC2180) "Image-Guided and Functionally Instructed Tumor Therapies", Eberhard Karls University Tuebingen, Tuebingen, 72076 Germany.

[6]Department of Biomedical Engineering, Eberhard Karls University Tuebingen, 72076 Tuebingen, Germany.

[7]Department of Medicine/Cardiology, Cardiovascular Research Laboratories, David Geffen School of Medicine at UCLA, Los Angeles, CA, 90095 USA.

* Nicole Anderle, Christian Schmees
Email: nicole.anderle@nmi.de, christian.schmees@nmi.de

Abstract

In light of the frequent development of therapeutic resistance in cancer treatment, there is a strong need for personalized model systems accurately representing tumor heterogeneity, while enabling parallel drug testing and prediction of appropriate treatment responses in individual patients. Using ovarian cancer as a prime example of a heterogeneous tumor disease with complex microenvironment, we demonstrate the efficient isolation of highly viable patient-derived microtumors (PDM). Importantly, our data demonstrate histopathological comparability of ovarian cancer PDM with corresponding patient tumor tissue. The establishment of Reverse Phase Protein Array (RPPA)-based analyses of >110 total and phospho-proteins using small amounts of PDM enabled the identification of sensitivities to standard, platinum-based as well as experimental, selumetinib-based therapy, and thereby the prediction of treatment-responders. Strikingly, clinical follow-up of corresponding patients confirmed significantly increased metastasis-free survival of identified carboplatin-responders. Finally, combining PDM and autologous TILs for individual efficacy testing of immune checkpoint inhibitors demonstrated the potential for patient-specific enhancement of cytotoxic TIL activity by this therapeutic approach.

Teaser

Microtumors represent the cellular complexity of individual patient tumors and enable treatment response prediction.

Main Text

Introduction

In the context of personalized medicine, patient-derived model systems are expected to play an important role in order to identify suitable and effective therapies for the individual patient as well as existing therapeutic resistances of the patient's tumor. Especially for cancer types with dismal treatment success rates such as ovarian cancer (OvCa), these model systems will be of great importance for future cancer treatment. OvCa is among the most lethal gynecological diseases in women with >185.000 deaths worldwide in 2018 (*1*). Late diagnosis and disease complexity characterized by strong molecular and genetic heterogeneity are causative for its poor survival rates and varying treatment response to first-line therapy. Substantial efforts have been made to resolve the complexity of OvCa, especially for high-grade serous carcinomas (HGSC) (*2-4*). Despite the application of genomics and transcriptomics in elucidating disease determinants, the principles of responsiveness to therapy are still poorly understood (*4*). The establishment of patient-derived tumor organoids (PDO) allowed addressing a number of these challenges for example by in-depth genetic and phenotypic tumor characterization and analysis of intra-tumoral heterogeneity in PDOs side-by-side with corresponding tumor tissue (*5-8*). Even though recent studies have described the combination of PDO cultures with components of the tumor microenvironment including fibroblasts, endothelial cells and immune cells (*9*), PDOs do not reflect the original composition of primary tumor tissue in terms of extracellular matrix, tumor-associated fibroblasts, tumor-infiltrating lymphocytes (TILs), macrophages (TAMs), and tumor endothelial cells. Another challenge of current PDO models in terms of applicability for individualized tumor response testing relates to the required establishment time of 1-3 months with a corresponding impact on the timeframe to obtain drug testing results (*10*). Using OvCa as a prime model of a heterogenous tumor disease, we introduce a three-dimensional (3D) preclinical model composed of patient-derived microtumors (PDM) as well as autologous tumor-infiltrating lymphocytes (TIL) isolated from primary OvCa tissue specimen in a clinical relevant time-frame. Importantly, PDM recapitulate a 3D histo-architecture with retained cell-cell contacts and native intra-tumoral heterogeneity featuring the corresponding primary tumor microenvironment (incl. extracellular matrix proteins, stromal fibroblasts and immune cells). In combination with functional compound efficacy testing and multiplexed TIL phenotyping, we demonstrate the correlation of individual OvCa PDM responses to chemotherapeutic targeted as

well as immunotherapeutic treatment approaches using OvCa PDM alone and in co-culture with autologous TILs, respectively. We used Reverse Phase Protein Array (RPPA) analysis to map protein-signaling pathways of PDM and to measure on- and off-target pathway effects in compound treated PDM. Strikingly, a correlation of obtained data in OvCa PDM models with clinical follow-up data of corresponding patients showed a significant increase in metastasis-free survival of identified carboplatin-responders as compared to non-responders.

Based on the data presented here, we envision that our preclinical assay system combining PDM, autologous TILs and protein signaling pathway profiling may in the future be used for the prediction of individual treatment responses and could therefore assist in the pre-selection of a personalized clinical treatment strategy for OvCa.

Results

Isolation of highly viable patient-derived microtumors from primary OvCa tissue samples by limited enzymatic digestion

Residual fresh tumor tissue samples were collected from n = 19 patients suffering from OvCa and undergoing primary tumor debulking surgery. Available, anonymized clinicopathological characteristics including International Federation of Gynecology and Obstetrics (FIGO) staging and pathological TNM-classification of respective individuals are summarized in Table S1. 2/19 patients (OvCa #4 and OvCa #18) received neoadjuvant treatment with carboplatin/paclitaxel chemotherapy. The majority of included samples (n = 17) were derived from the most common type of OvCa, i.e. epithelial OvCa, with a majority of high-grade serous carcinomas (HGSC). Two samples were classified as sex-chord-stromal ovarian carcinomas that are either non-malignant or at a low stage. PDM isolation adapted from Kondo *et al.* 2011 (*11*) and TIL isolation was performed on freshly excised tumor tissue specimen. Isolation of PDM amounts suitable for downstream analyses was successful in >70% (14/19) of the tumor samples (Fig. 1A). PDMs were cultured in suspension in the absence of serum for a maximum of three weeks. No correlation was observed between successful isolation of PDM and available clinical patient data such as age, lymph node spread, distant cancer spread, perineural invasion or FIGO stage (Table S2). PDM viability was assessed by parallel staining with Calcein-AM and SYTOX™ Orange (Fig. 1B). 2D projections of 3D images displayed highly viable PDM with few dead cells. Dead PDM cells (according to nuclear SYTOX™ Orange staining) were detached from PDM and thus observed mostly as single cells floating in the culture media. The quantification of the viable cell volume and dead cell volume in 3D projections of four exemplary OvCa PDM models are shown in Fig. 1C. In each analyzed model, ≤ 7% of the total PDM cell mass represented dead cells confirming robust PDM viability.

OvCa PDM sections resemble histopathological characteristics of the corresponding primary tumor tissue (PTT)

We next performed Hematoxylin and Eosin staining (H&E) of FFPE- and cryosections, respectively, derived from OvCa PDM and corresponding primary tumor tissue sections (PTT) for histopathological comparison. Professional assessment of PDM by a certified pathologist, confirmed typical, distinct histopathological characteristics of OvCa (Fig. 1D and Fig. S1). HGSC derived PDM reflected architectural patterns such as papillary growth, irregular branching, cystic and glandular structures (Fig. 1D OvCa #17-23; Fig. S1, OvCa #24, 26) as compared to the corresponding PTT specimen. Pleomorphic nuclei/cells, high nucleus:cytoplasm ratio as wells as hyperchromasia were similar in PDM and corresponding PTT sections reflecting the high-grade of analyzed HGSC tumors. These tumor features were not detected within OvCa PDM #8 (Fig. S1), which originated from low-grade mucosal OvCa known for slow tumor growth. Instead, OvCa #8 PDM displayed a unicellular epithelium and mostly stromal remains. In summary, histopathological analyses of PDM confirmed structural and cellular similarities to the

corresponding primary tumor specimen resembling typical histological features of ovarian carcinomas.

PDMs reflect intra- and intertumoral heterogeneity of the original tumor

For further characterization and study of the similarity of OvCa PDM and corresponding PTT, the expression of histotype specific markers, different tumor cell-, extracellular matrix- and immune cell-markers were assessed by immunohistochemistry (Fig. 1D, Fig. S1). In the clinics, immunohistochemical staining of p53 and Wilms Tumor 1 (WT1) is applied for differential diagnosis of HGSCs (*12*). HGSC phenotype of the original tumor persists in the corresponding PDM as marker expression of WT1/p53 highly corresponded with either low-to-moderate (OvCa #17-18) or strong expression (OvCa #23). Mesothelin (MSLN) and CA125 (MUC16) were used as additional OvCa markers. Mesothelin, known to be over-expressed on the cell surface in OvCa (*13-15*), was readily expressed in OvCa PDM resembling expression of this marker in their corresponding PTT. Besides MSLN, CA125 expression has previously been described as an immunohistochemical marker to confirm ovarian origin of the tumor (*16*). As shown before (*17, 18*), expression of CA125 in OvCa sections can vary within one type and between the different OvCa tumor types. Accordingly, PTT sections derived from non-HGSC displayed no CA125 expression (OvCa #8) in contrast to HGSC-derived tumor sections (OvCa #17-18, #23-26). In PDM models OvCa#8, #17, #18 and #24 staining patterns of MSLN and CA125 were similar to corresponding PTT sections and were often restricted to cells at the tumor margin for CA125 (e.g. OvCa #18, #23). As the tumor microenvironment is known to play a major role in tumor progression and metastasis (*19-21*), we analyzed the presence of extracellular matrix (ECM) and stromal components in OvCa PDM and corresponding PTT. Sections were stained for FAPα (Fibroblast associated protein alpha), a marker of activated fibroblasts, also known as cancer-associated fibroblasts (CAFs). FAPα expression in tumor stroma is observed in 90% of human cancers of epithelial origin and has been described to induce tumor progression and chemoresistance (*22*). FAPα staining in OvCa PDM mostly resembled that of the corresponding PTT in all samples except for OvCa #24-26 and differed from low to high expression. Collagen I expression, known to promote invasiveness and tumor progression in epithelial OvCa (*23*), was also prominent within OvCa PDM. Stainings correlated with corresponding PTT that showed an overall strong Collagen I expression except for OvCa #25. We also observed a strong correlation of Hyaluronan Binding Protein 1 (C1QBP) expression in PDM and corresponding PTT, which interacts with the major ECM component hyaluronan (*24*). In summary, all studied stromal components were found to be highly abundant within OvCA PDM and corresponding PTT. To further examine tumor microenvironmental (TME) components of PDM, we studied the infiltration with tumor-associated macrophages (TAMs) via CD163 expression together with the expression of the inhibitory checkpoint receptor ligand PD-L1. Analysis rarely detected M2-like TAMs ($CD163^+$) within PTT and PDM sections and if so, mostly in stromal tissue parts. While macrophages were highly frequent in OvCa #24 PTT, they were not detected in the corresponding PDM (Fig. S1). In contrast, for OvCa #17, $CD163^+$ TAMs were detected in both PDM and PTT sections (Fig. 1). Immune checkpoint receptor ligands are known to be expressed on tumor and/or immune cells of the tumor microenvironment. Here, PD-L1 expression was mostly absent in OvCa PTT and corresponding PDM sections. In conclusion, PDM largely resembled features of the original tumor by direct comparison with corresponding PTT including presence of complex ECM and TME architecture and expression of markers specific for OvCa. In comparison with corresponding PTT sections, pure stromal areas were mostly absent from stained PDM sections, which might explain differences observed between PDM and corresponding PTT with regard to immune cell infiltration and degree of expression of stromal components.

Protein signaling pathway profiling of OvCa PDM by RPPA

After initial immunohistochemical characterization of the 3D OvCa PDM that confirmed the presence of TME components in PDM similar to corresponding PTT, we performed an in-depth examination of the heterogeneity and molecular composition of different OvCa PDM models by generating complete signaling pathway protein profiles using RPPA. Protein abundances of 116 different proteins (including total and post-translationally modified forms) were measured in OvCa PDM samples each with a sample size of n = 100-150 per individual PDM (Fig. 2A). One further PDM sample derived from human BC (breast cancer) was included to scale up the protein sample data and for comparison as both cancer types are known to share molecular and microenvironmental similarities (*21, 25*). Obtained protein-normalized, background-corrected mean fluorescence intensity (NFI) signals were median-centered to all samples (n = 8) and $\log_2$ transformed. Protein profiles of PDM samples covered signaling pathways such as for cell cycle, DNA damage response, apoptosis, chromatin regulation, MAPK/RTK, PI3K/AKT with mTOR, Wnt and NFκB, as well as OvCa tumor/stem cell markers. By hierarchical clustering (HCL), PDM were grouped according to their similarities in relative protein signal intensity (Fig. 2A). Data analysis revealed three clusters: 1) OvCa #21 (OvCa granulosa cell tumor) and #23 (HGSC), with the most distinct protein profiles as compared to the other PDM analyzed; 2) OvCa #19 (HGSC) and the BC PDM shared more similarities then OvCa #19 with the other OvCa PDM models; 3). The remaining PDM samples resembled the third cluster with the most similar protein expression profiles containing exclusively HGSC models. Long distances of the sample dendrogram further underlines the proteomic heterogeneity of similar histopathological OvCa tumor types.
To compare protein abundances within different signaling pathways as well as of tumor/stem cell markers, proteins with impact on pathway activity were sorted according to their pathway affiliation (Fig. 2B, Table S3). Significant differences between PDM models were observed for the cell cycle pathway and the MAPK/RTK pathway. Highest cell cycle activity was found in OvCa #17 and #24 with almost 50% higher median NFI signals compared to OvCa #21 with the lowest median signals (median NFI = -0.33 $\log_2$) resembling a different histopathological tumor type compared to the other PDM models analyzed. MAPK/RTK pathway signaling was increased in OvCa #21 (median NFI = 0.38 $\log_2$), #23 (median NFI= 0.32 $\log_2$), #24 (median NFI = 0.31 $\log_2$) and #17 (median NFI = 0.30 $\log_2$). The BC PDM model was characterized by decreased median NFI signals of MAPK/RTK proteins (median NFI = -0.47 $\log_2$). Proteins related to PI3K/AKT pathway and of associated pathways were more abundant in OvCa #17 and #24. mTOR pathway levels were elevated in OvCa #24 (median NFI = 0.54 $\log_2$) in other OvCa PDM this pathway showed comparable activity. Median NFI signals from apoptosis-related proteins were significantly different between OvCa #25 (median NFI = 0.75 $\log_2$) and BC PDM (median NFI= 1.41 $\log_2$). OvCa tumor/stem cell marker protein abundance was significantly upregulated in both OvCa #17 and #23 compared to BC PDM. RPPA protein profiling analysis demonstrated the heterogeneous activity of several signaling pathways within different OvCa PDM. Apoptosis-related proteins and OvCa tumor/stem cell marker proteins indicated the strongest differences between OvCa PDM models and the BC PDM model.

Heterogeneous treatment responses towards chemo- and targeted therapy assessed by functional compound testing in OvCa PDM

Next, we used OvCa PDM as a platform for functional compound testing using standard-of-care chemotherapy treatment and targeted therapies. Further, we sought to relate treatment responses in PDM to the generated protein profiling datasets. Studies of targeted therapies in OvCa are often limited to clinical phase I and II or even cell-line based preclinical studies (*26-28*), as treatment efficacies are heterogeneous and mostly not beneficial compared to standard chemotherapy. However, targeting specific signaling pathways could demonstrate a treatment alternative for individual OvCa patients either as first-line or recurrent-cancer therapy. As we have discovered that protein abundances differed the most in the cell cycle and MAPK/RTK pathway in OvCa PDM (Fig. 2A-B), we investigated efficacy of targeted inhibition of these pathways with the

CDK4/6 inhibitor palbociclib, the MEK1/2 inhibitor selumetinib, as well as the Src-inhibitor saracatinib and compared these treatments to standard platinum-based chemotherapy (Fig. 2C). PDM were treated with respective drugs, each at three different concentrations, chosen according to previously reported C_{max} concentrations (*29*). Treatment efficacy in OvCa PDM – as measured by cytotoxicity - was heterogeneous among individual PDM models, with some specifically responding to carboplatin (most prominently OvCa #24) and others to targeted therapy (OvCa #19, #21, #26). Carboplatin induced the most significant cytotoxic effects at the lowest dose (75 µM) at longest duration t = 72 h in OvCa #17 and #24 (Fig. 2C). On the molecular level, RPPA protein profiling revealed significantly increased cell cycle activity in both models (Fig. 2B), which might be associated with the stronger carboplatin response observed in OvCa PDM #17 and #24. Two other PDM models were also carboplatin sensitive, but responded to treatment at higher dose (OvCa #23, #25). Accordingly, both had shown intermediate cell cycle activity in protein profiling analyses (Fig. 2A-B). Selumetinib induced significant cell death in OvCa #17, #19, #21 and #23 at a final concentration of 100-150 nM (Fig. 2C). The strongest effect was observed for OvCa #21, which displayed comparatively high MAPK/RTK pathway activity (Fig. 2B). Palbociclib, an inhibitor of G1-cell cycle progression, caused significant cytotoxicity in OvCa #25 and #26, which both had shown moderate cell cycle activity in RPPA protein analysis (Fig. 2B). PDM models with significantly higher cell cycle activity as measured by RPPA (OvCa #17, #24), did not respond to palbociclib treatment. Inhibition of the Src-pathway by saracatinib caused significant and dose-dependent killing effects in OvCa #26. Saracatinib triggered rapid PDM death already after 24-48 h of treatment. In conclusion, functional compound testing further confirmed the molecular heterogeneity of studied OvCa PDM models identified by protein profiling. Interestingly, PDM models showing resistance to standard chemotherapy with carboplatin were instead sensitive towards targeted therapeutic approaches.

Correlation of treatment response and activation state of protein signaling pathways

To relate the analyzed protein signaling pathways of untreated OvCa PDM to observed treatment responses, protein NFI signals of PDM were grouped into responder and non-responder profiles according to results from functional compound testing (Fig. 2C, Fig. S2). Significant differences of pathway signaling in carboplatin/selumetinib responder and non-responder models were analyzed. Further, we examined the on- and off-target pathway effects within different OvCa PDM models by RPPA to assess drug mode-of-action (Fig. 3). For this aim, OvCa PDM were treated at one compound concentration and compared to vehicle (DMSO) control. Treatment-to-control signal ratios (TR) were determined from protein NFI signals of treated PDM samples and DMSO vehicle controls at three different time points for each treatment: immediate (30 min), early (4 h) and late (72 h). This enabled the exploration of fast and late treatment response based on changes of protein abundances within a given time frame.

Carboplatin treatment sensitivity of OvCa PDM correlates with high protein abundance of G2-M cell cycle proteins

HCL clustering of PDM protein NFI signals led to five clusters that distinguish carboplatin sensitive and resistant PDM models (Fig. S3A). To analyze significant differences related to activation or inactivation of signal transduction pathways, proteins from the HCL clustering were sorted according to their pathway affiliation and according to upregulation or downregulation in responder. Carboplatin-responder showed significantly increased cell cycle activity ($P < 0.001$; Fig. 3A) with upregulated protein abundance observed for Aurora A kinase (mean NFI = 0.74 log_2), CDK2 (mean NFI = 0.8 log_2), Cyclin B1 (mean NFI = 0.84 log_2), PCNA (mean NFI = 0.84 log_2), and acetylated Tubulin (mean NFI = 0.1 log_2) (Fig. S3B), which are mostly related to "mitosis" (*30, 31*). Aurora A (Spearman's r = 0.912, $P = 0.022$), Cyclin B1 (Spearman's r = 0.971, $P = 0.011$) and PCNA (Spearman's r = 0.912, $P = 0.022$) significantly correlated with carboplatin treatment sensitivity (Table S4), which was graded according to recorded significance levels from 0-3 ("0": $P > 0.05$; "1": $P < 0.05$; "2": $P < 0.01$; "3": $P < 0.001$) (Fig. S2). At the same time, non-

responder showed higher abundance of CDK1 (mean NFI = 0.38 log_2), phospho-CDK2 (mean NFI = 0.77 log_2) and phospho-CDK4 (mean NFI = 0.37 log_2) (Fig. S3C), which are more related to the G0/G1 cell cycle phase. In addition, the apoptosis/DNA damage response pathway was significantly upregulated in responder OvCa PDM models compared to non-responder (P = 0.021; Fig. 3A), especially with high abundance of cleaved Caspase-8 and cleaved PARP (Fig. S3B). Additional significant differences between responder and non-responder OvCa PDM were detected within the RTK and the PI3K/AKT/NFκB signaling pathways (P < 0.001; Fig. 3A). These pathways were downregulated in the non-responder group. Higher EMT/tumor/CSC marker abundance was significantly associated with the carboplatin responder group (Fig. 3A). Markers included Mesothelin, Nanog, STAT1, and E-Cadherin (Fig. S3B). In contrast, there were few proteins found, which were downregulated in the responder group. Collectively, this panel of downregulated proteins differed significantly compared to the non-responder group (Fig. 3A). It contained early cell cycle markers e.g. Aurora A and Cyclin B1, the mTOR pathway effector phospho-S6RP, PDGFR and SNAI1 (Fig. S3C). In summary, the activation state of different signaling pathways comprised of proteins with >20% difference in abundance, allowed to significantly distinguish carboplatin responder from non-responder OvCa PDM models.

Carboplatin treatment is associated with early induction of stress-response and late apoptosis

Next, we sought to investigate the carboplatin drug mode-of-action within OvCa PDM. Therefore, the carboplatin-responding OvCa PDM #24 was treated with carboplatin at a concentration of 75 µM, which had significantly induced PDM cytotoxicity (see Fig. 2C). Protein NFI signals were measured at three different time points and normalized to vehicle control. Proteins revealing >50% difference in TR signals (Fig. S4) were selected to focus on the strongest changes in abundance. Cell cycle progression proteins (phospho-CDK2, CDK1) and phospho-Histone H3 (Ser10), affecting chromatin condensation during cell division, were downregulated quickly within 30 minutes (Fig. 3B). After 4 h of treatment, TR signals of phospho-Aurora A/B/C protein and Histone H3 was strongly increased (Fig. S4). Longer incubation with carboplatin (72 h) resulted in strong downregulation of these proteins (Fig. 3B). Diminished abundance of cell cycle proteins after 72 h of carboplatin treatment differed significantly from vehicle control (P < 0.001) and from early treatment (4 h; P < 0.001). While levels of cell cycle related proteins decreased over time, apoptotic markers such as cleaved-Caspases as well as acetylated p53 were elevated after 72 h (Fig. S4). Induction of apoptosis-related proteins was already observed after 4 h of treatment (Fig. 3B) with increasing abundances of cleaved Caspase 7 and acetylated p53 (Fig. S4). Focusing on down-stream PI3K/AKT/mTOR/Wnt pathway regulation, the abundances of mTOR effector proteins (S6RP, S6RP-phospho) were quickly upregulated after immediate (0.5 h) carboplatin treatment (Fig. S4), which is in line with previous reports about transcriptional regulation of stress response by the mTOR pathway (*32*). We also observed additional elevation of mTOR pathway-related proteins after 4 h of carboplatin treatment. Furthermore, overactive mTOR signaling might have resulted in increased p53 activation through increased acetylated p53 levels (Fig. S4) as described before (*32*). The PI3K/AKT/mTOR pathway was significantly upregulated within 4 h of carboplatin treatment compared to vehicle control (P = 0.021; Fig. 3B). Similar to proteins related to cell cycle, this pathway was completely abrogated as compared to vehicle control after 72 h of treatment (P < 0.001; Fig. 3B). Changes in protein abundance differed significantly during all three measured time points (0.5 h vs. 4 h: P = 0.003; 4 h vs. 72 h and 0.5 h vs.72 h: P < 0.001 Fig. 3B). Complete, significant downregulation of MAPK/RTK pathway occurred after 72 h of treatment (P = 0.017; Fig. 3B). The proteomic changes within MAPK/RTK-related proteins over time were significant (0.5 h vs. 4 h: P = 0.009; 4 h vs. 72 h: P < 0.001; Fig. 3B). Thus, carboplatin treatment of OvCa #24 illustrated substantial and time-dependent changes in TR signals. Short treatment with carboplatin apparently triggered the induction of stress responses while longer treatment duration caused the induction of apoptosis.

Metastasis-free-survival prolonged in carboplatin responder group

To assess the predictive value of OvCa PDMs and obtained drug testing data, we compared metastasis-free-survival (MFS) between carboplatin responder (OvCa #17, #23-25) and non-responder (OvCa #19, #26) (Fig. S5). For this, OvCa PDM models were classified according to carboplatin-responses measured by PDM functional compound testing (Fig. S2). Following consideration of clinical follow-up patient data survival analyses revealed a significant difference between carboplatin responder and non-responder. Carboplatin-responder had a prolonged median MFS of 494 days (16.2 month) versus 281 days (9.2 month) in non-responder. Thus, functional compound testing of OvCa PDM might enable treatment response prediction of platinum-based standard chemotherapy in corresponding ovarian cancer patients.

Selumetinib responding OvCa PDM models display increased MAPK/RTK pathway activity

HCL cluster analysis by Euclidean distance distinguishes selumetinib responder and non-responder OvCa PDM models by six clusters (Fig. S6A). By sorting these proteins according to pathway affiliation, selumetinib responder PDM models showed significantly increased MAPK pathway (e.g. Erk1/2) and RTK pathway proteins (e.g. PDGFRβ) compared to non-responder PDM in line with previous reports from cell line-based studies (*33*) ($P < 0.001$; Fig. 3C and Fig. S6B). Another protein cluster consisting of diverse pathway proteins such as the cell cycle, EMT markers or tumor markers showed significantly higher NFI signals compared to non-responder PDM models ($P < 0.001$; Fig 3C and Fig. S6B). In contrast, one cluster was defined by increased NFI signals within non-responder PDM with significantly upregulated proteins related to cell cycle/DNA damage response (e.g. cleaved Caspases, phospho-CDK4), MAPK signaling (phospho-EGFR (Tyr1068)), PI3K/AKT signaling and associated pathways such STAT and Wnt signaling ($P < 0.001$; Fig. 3C and Fig. S6C). Similar to previous cell line studies (*33, 34*) we detected a number of potential selumetinib resistance features such as high levels of phospho-EGFR (Tyr1068) and an active PI3K/AKT pathway in non-responder PDM models. By grouping the proteins from HCL clustering according to pathway affiliation and abundance levels, we were able to distinguish responder from non-responder PDM models. Especially a more active MAPK/RTK pathway and a less active PI3K pathway allowed for the differentiation of responder from selumetinib-resistant, non-responder PDM models.

Upregulation of MAPK/RTK and PI3K/AKT signaling pathways in response to selumetinib treatment as a potential resistance mechanism

We next evaluated on- and off-target pathway effects by RPPA protein profiling of selumetinib-treated OvCa models to assess potential resistance mechanisms. As data were available from selumetinib responder (OvCa #17 and #21) and non-responder (OvCa #24) PDM models, protein abundances after treatment were compared for those groups. Protein abundances were measured as TR signals at three different treatment durations to track protein changes over time (Fig. 3D). Proteins with 100% differential mean TR signals between these groups were selected (Fig. S7-S9) and sorted according to pathway affiliation. While shortly after 4 h of treatment responder PDM models upregulated specific cell cycle and apoptosis proteins (Fig. 3D) incl. cleaved Caspase 7, phospho-CDK2 ($P = 0.017$) and phospho-Histone H3 (Ser10) (Fig. S7), non-responder PDM models significantly upregulated cell cycle proteins after 72 h of treatment ($P < 0.001$; Fig. 3D). Proteins showing increased abundance are involved in G0/G1- and G2/M-cell cycle progression such as Aurora A, phospho-CDK4, phospho-CDK6, phospho-Rb, phospho-CDK2 (Fig. S7). In contrast to a progressing cell cycle within non-responder PDM models, selumetinib induced a cell cycle arrest and apoptosis in the responder PDM group accompanied by upregulation of phospho-CDK2 (*35*), the effector cleaved Caspase 7 and p53 (Fig. S7). After 72 h of treatment, analyses identified a significant difference in the activity of the MAPK/RTK pathway, which was directly affected by the treatment with the MEK1/2 inhibitor ($P = 0.004$; Fig.

3D). Treatment did not affect the MAPK/RTK pathway activity in the non-responder group. Instead, our data showed a time-dependent increase in MAPK/RTK activity (Fig. 3D, S8). In line with reports about the influence of PI3K/AKT/NFκB/Wnt signaling on resistance to selumetinib treatment in cell lines (*33, 34, 36*), we detected a significant upregulation of proteins related to these pathways within the non-responding OvCa PDM after 4 h ($P = 0.003$) and 72 h ($P < 0.001$) of treatment (Fig. 3D, S9). Non-responder PDM models showed a downregulation of the AKT-inhibitor PTEN over time accompanied by increased phospho-AKT and Wnt signaling proteins such as β-catenin, phospho-GSK3β (Fig. S9). At the same time, PI3K/AKT/NFκB/Wnt signaling proteins were substantially decreased following selumetinib treatment in responder PDM models (Fig. 3D). Thus, parallel upregulation of PI3K/AKT/NFκB/Wnt and MAPK/RTK signaling might illustrate a potential resistance mechanism in selumetinib non-responder OvCa PDM models.

Characterization of tumor-infiltrating lymphocyte populations from primary OvCa tissue samples

Our established procedure of tissue processing and PDM isolation enabled us to obtain single-cell suspensions containing tumor-infiltrating lymphocytes (TILs) from respective OvCa tumor specimen. This allowed for expansion of these autologous TILs in the presence of low-dosed cytokines and antigenic stimulation in order to investigate the immunogenicity of our patient samples. The immunogenicity of OvCa has been demonstrated in prior studies and is confirmed by the frequent infiltration of ovarian tumors with TILs (*37-39*). As reported by Sato *et al*. (2005), different T cell populations diversely influence tumor immunosurveillance in OvCa. High intraepithelial $CD8^+/CD4^+$ T cell ratios in patients were associated with improved survival as $CD4^+$ T cells executed immunosuppressive functions. To determine the composition of the isolated immune cell infiltrate within our sample cohort, we characterized the phenotype of autologous TIL populations by multi-color flow cytometry (Fig. S10A). Within isolated and expanded OvCa TIL populations from different specimen, we found that the proportion of $CD4^+$ TILs was 57.8% and significantly more abundant than $CD8^+$ TILs with 33.5% ($P = 0.003$**; Fig. 4A, Table S5). As higher CD8:CD4 ratios were previously correlated with better survival in OvCa patients (*37, 39*), the majority of patients in this cohort were characterized rather with an unfavorable prognosis (Fig. S10B).

Isolated $CD8^+$ OvCa TILs are comprised of tumor-specific $CD39^+$, stem-like $CD39^-PD1^+$ and terminally differentiated $CD39^+PD1^+$ populations

Within the isolated $CD8^+$ TIL populations, we identified different phenotypes according to expression of the co-inhibitory receptors PD-1 and CTLA-4, the tumor-antigen specificity marker CD39 and the activation marker CD137 (Fig. 4A). To investigate the activation status of $CD8^+$ TILs, cells were examined for co-expression of the co-stimulatory receptor CD137 (4-1BB). CD137 is upregulated in activated T cells and has been suggested to be a marker for antigen-activated T cells (*40*). The mean percentage of $CD8^+$ $CD137^+$ TILs was 3.1% and varied between 0-10% (Table S5). >5% of the $CD8^+$ cytotoxic T-cells (CTLs) from OvCa #1, #3 and #5 (Fig. S10B) co-expressed CD137 indicating their pre-exposure to tumor antigens. Expression of co-inhibitory receptors PD-1 and CTLA-4 on $CD8^+$ TILs did not differ significantly among analyzed TIL populations but tended to higher PD-1 expression levels (mean 6.9% vs. 3.4%; Table S5). TILs from OvCa #3, #7 and #25 as well as #5, #13 and #26 were among those displaying an exhausted phenotype with >10% of $CD8^+PD\text{-}1^+$ or $CD8^+CTLA\text{-}4^+$ TILs (Fig. S10). Moreover, in recent reports CD39 expression in $CD8^+$ TILs was described as a marker for tumor-antigen specific TILs that have undergone tumor-antigen-driven clonal expansion, exhibit resident memory T cell like phenotypes and express a variety of co-stimulatory and co-inhibitory receptors (*41-43*). Here, $CD39^+$ CTLs (mean 40.5%; range 4.4-96.8%, Table S5) were significantly more abundant than $CD39^-$ CTLs (mean 9.5%; range 0-48.3%, Table S5) so called 'bystander TILs' known to recognizing mostly viral antigens (*42*) ($P < 0.001$, Fig. 4A). The amount of $CD39^+$ TILs strongly correlated with the amount of $CD8^+$ TILs (Spearman $r = 0.88$, Fig. S10C; $P < 0.001$,

Table S6) and conversely with the amount of $CD4^+$ TILs (Spearman r = -0.80, Fig. S10C; P = 0.002, Table S6). Thus, the abundance of $CD4^+$ and $CD8^+$ TILs appeared to significantly determine the amount of $CD39^+$ CTLs. In addition, CD39 expression was largely limited to $CD8^+$ TILs. As co-inhibitory receptors play a role in T cell exhaustion and are important targets for immune checkpoint-inhibition, we analyzed PD-1 and CTLA-4 expression on the tumor-specific $CD39^+$ CTL population. $PD1^+CD39^+$ were more frequent than CTLA-4^+ $CD39^+$ (15.7% vs. 5.4% Fig. 4A, Table S5). The total amount of $CD8^+PD1^+$ TILs thereby correlated with the amount of $CD8^+CD39^+PD1^+$ TILs (Spearman r = 0.79, Fig. S10C; P = 0.002, Table S6) of a PDM model. Thus, CD39 expression was limited to tumor-antigen stimulated and exhausted TILs (e.g. OvCa #7, #17 and #25; Fig. S10B). In contrast to 'terminally differentiated cells' (*44*), OvCa TILs with a 'stem cell-like' $CD39^-PD1^+$ phenotype were found in 7.3% of the CTLs (Table S5). This population showed the highest proportional variability with a maximum of 50.5% cells vs. a minimum of 0% as compared to other $CD8^+$ TIL populations (CV 208%). The frequency of $CD8^+CD39^+$ and stem cell-like $CD8^+CD39^-PD1^+$ was negatively correlated (Spearman r = -0.63, Fig. S10C; P = 0.024, Table S6).

Specific TIL phenotypes isolated from OvCa tumor specimen correlate with regional lymph node metastasis

We further analyzed the correlation between specific TIL populations and clinical follow-up patient data. OvCa patients with regional lymph node metastasis (N = 1) tended to present with significantly more extensive $CD8^+$ TIL infiltration in their tumors than those with no lymph node metastasis (N = 0) (P = 0.016) (Fig. 4B). As the frequency of $CD8^+$ TILs was shown to significantly correlate with that of $CD8^+CD39^+$ TILs in OvCa (Fig. 4B), our data implicate a significant correlation between lymph node spread (N=1) and the presence of a $CD8^+CD39^+$ population (P = 0.008).

OvCa PDM killing by autologous TIL populations is enhanced by immune checkpoint inhibitor treatment

To evaluate the functional, tumor cell killing capacity of autologous TILs on OvCa PDM and the corresponding treatment efficacy of established immune checkpoint inhibitors (CPI), we subjected co-cultures of TILs and PDM from OvCa #24 and #26 to image-based analysis of CPI-treatment response. A total of nine PDM were imaged per treatment (3 PDM per well in triplicates) and a dead:live PDM ratio was calculated according to the sum of measured fluorescent intensities (FI) (Fig. 4C-E). Addition of TILs to autologous PDM induced a basal killing effect in PDM in both models analyzed in the absence of CPI treatment (Fig. 4D-E). For both co-culture models analyzed, the addition of CPI led to an increase in PDM cell death. Significantly higher killing effects in OvCa #24 co-cultures were observed in response to treatment with either the combination of anti-PD1 and anti-CTLA-4 (pembrolizumab + ipilimumab) or anti-PD-L1 and anti-CTLA-4 (atezolizumab + ipilimumab) (P = 0.039) compared to isotype control treatment (Fig. 4D). As the addition of isotype controls showed no additional effect in both co-culture models, we excluded the possibility of unspecific killing effects of CPI antibodies. CPI treatment almost doubled PDM killing in OvCa #26 (Fig. 4E). In comparison, co-cultures treated with ipilimumab (P = 0.004) or atezolizumab (P < 0.001) showed significant PDM killing compared to untreated PDM. The killing effect of TILs was significantly amplified by atezolizumab treatment as compared to co-culture controls (PDM+TIL: P = 0.021; PDM+TIL+IgG4: P = 0.018; Fig. 4E). Further, atezolizumab treatment significantly increased the TIL killing effect towards PDM as compared to pembrolizumab (P = 0.026). Taken together, autologous TILs from both OvCa PDM models studied were composed of high amounts of tumor-specific, non-terminally differentiated $CD8^+CD39^+$ TIL populations (Fig. S10B) inducing PDM killing. Especially TILs from OvCa #26 responded with enhanced PDM killing to CPI treatment. Thus, co-culture assays of autologous TILs and PDM offer a platform to assess CPI treatment efficacies in a preclinical, patient-specific setting.

Discussion

Recently we could show the establishment of PDM from human glioblastoma tissue specimen containing important components of the tumor stroma (e.g. tumor-associated macrophages), and their application for the assessment of responses towards CSF1R- and PD1-targeting antibodies as well as the small molecule inhibitor Argyrin F (*45, 46*). In the present study, we have now further extended this approach to a patient-derived model system consisting of PDM and autologous TILs extracted from a panel of primary OvCa tissue specimen and their in-depth characterization by immunohistochemistry, protein profiling, immune cell phenotyping and focused compound efficacy testing. Our results show a 70% success rate for isolation of PDM with robust viability and in suitable amounts for further, multi-parametric downstream analyses. In-depth histopathological assessment of PDM sections confirmed the conservation of typical histological features of respective OvCa types by this model system. Importantly, the complexity of the ovarian cancer TME with respect to the presence of cancer-associated fibroblasts and extracellular matrix components incl. collagen and hyaluronan-binding protein observed in primary OvCa tissue sections was well reflected in PDM. The presence of these TME components has previously been correlated with tumor stage, prognosis, and progression and shown to substantially influence treatment responses (*23, 47, 48*). Interestingly, we could also identify immune cell infiltration within a subset of OvCa PDM, reflecting the immunogenicity of OvCa as previously reported (*37, 38, 49*).

While OvCa patient-derived organoids (PDO) were often studied by genomic and transcriptomic sequencing (*6-8*), we were the first (to our knowledge) to investigate inter-tumoral heterogeneity and differential drug response mechanism by RPPA-based protein profiling in a patient-derived 3D OvCa preclinical model. Here, analyses of a panel of >110 phospho- and total proteins allowed for the clustering of histologically similar OvCa PDM models, pathway activity profiling and investigation of on- and off target drug effects. Obtained RPPA protein profiles confirmed the heterogeneity of OvCa PDM observed via immunohistochemistry and previously reported for HGSC, the most common type of OvCa. Our work identified significant differences in the activity of cell cycle and MAPK/RTK pathways within analyzed OvCa PDM and enabled their distinction from a breast cancer derived PDM model by differential expression of OvCa tumor and stem cell markers as well as apoptosis-related proteins.

Seven OvCa PDM models were applied for individualized compound efficacy testing using a panel of clinically approved drugs at C_{max} drug concentrations previously reported in clinical trials. For analyzed OvCa PDM models, we observed patient-specific heterogeneity of response towards chemotherapy and targeted therapy. Correlation with RPPA protein profiling data allowed the allocation of individual PDM drug responses to specifically up- or down-regulated signaling pathway activities and, importantly, enabled the prediction of PDM models with high probability of response towards chemotherapy or targeted therapy. In accordance with the ability of cytostatic drugs to induce apoptosis especially in actively dividing cells (*50*), our work identified additional correlation between proteins relevant for S- and G2/M- cell cycle phase progression and carboplatin response. Specifically, our data implicate that elevated abundances of Aurora A, Cyclin B1 and PCNA proteins may allow for identification of carboplatin treatment response. Furthermore and in line with previous reports, we confirmed that decreased DNA damage repair and the ability to undergo apoptosis (*51*) is associated with carboplatin treatment sensitivity in OvCa. This was illustrated by increased levels of cleaved Caspase-7 and cleaved PARP. Our results did not identify a correlation of carboplatin-resistance and markers of cancer stem cells (CSCs) (*52, 53*) or epithelial-to-mesenchymal transition (EMT) (*54, 55*). Instead, we found the cancer stem cell-related protein Nanog as well N-Cadherin strongly upregulated in carboplatin responding PDM. These differing results might arise from the fact that above-mentioned previous studies were performed in adherent cell lines and not within a patient-derived 3D tumor model. Importantly, we identified protein signatures of OvCa PDM allowing for the identification and prediction of PDM models with high probability of response towards chemotherapy or targeted therapy. Strikingly, our results showed a significant correlation of carboplatin treatment response with prolonged metastasis-free survival of respective patients.

The targeted inhibition of MEK1/2 kinase by selumetinib induced cell death within different OvCa PDM models. Treatment responses to selumetinib have yet been clinically evaluated with a focus on LGSC patients, because of observable MAPK pathway activation in this type of OvCa. However, reported clinical response rates were limited. Nevertheless, different studies identified relationships between phospho-EGFR (Y1068) and phospho-Erk with selumetinib sensitivity (*33, 34, 36, 56*). In line with this, our study identified selumetinib-sensitive PDM models by means of moderate MAPK/RTK pathway activity with increased abundance of Erk1/2, PDGFR and other proteins. Furthermore, our results imply a central role of active PI3K/AKT/mTOR signaling and upregulated caspase protein levels in selumetinib treatment resistance.
We further assessed proteomic changes upon PDM treatment such as effects on protein abundance, directed on- and off-target pathway effects and drug mechanism-of-action within OvCa PDM. In a carboplatin sensitive PDM model, we observed a time-dependent decrease in cell cycle- and an increase in apoptosis-inducing protein abundance. In parallel, we found a fast stress response upon treatment as indicated by an activated mTOR pathway with high S6RP and active phospho-S6RP levels (*32*). Overactive mTOR in combination with cell stress and the inability of cells to adapt to cellular stress might be responsible for p53 elevation (*57, 58*) and driving cells into senescence or apoptosis (*59, 60*). The degree of mTOR activation and the severity of stress in form of carboplatin-induced DNA damage might indicate the failure of PDM to induce protective responses and thus treatment-sensitivity.
With the comparison of on- and off-target pathway effects in selumetinib-sensitive and –resistant OvCa PDM models, we uncovered significant changes in protein abundance for responder versus non-responder PDM models during treatment. In line with previous reports, on-target pathway effects of selumetinib treatment were characterized by a reduction in MAPK/RTK pathway protein levels accompanied by the induction of cell cycle arrest and apoptosis by high cleaved Caspase7, p53 and phospho-CDK2 levels(*35*). Selumetinib treatment resistance was characterized on the one hand by MAPK feedback signaling with increased abundance of RTKs such as phospho-EGFR and upregulated AKT and Wnt-signaling by means of high phospho-AKT and β-catenin levels. Active PI3K/AKT/Wnt pathway signaling in OvCa PDM might indicate resistance to the MEK-inhibitor selumetinib as reported earlier (*33, 34, 36*).
Apart from testing the response of OvCa PDM to conventional therapy, we also applied immunophenotyping of autologous TIL populations followed by their co-culture with respective PDM for assessment of individualized responses towards immunotherapeutic mono- and combination treatment schedules. Immunosurveillance of cancer strongly depends on the composition of tumor-infiltrated immune cells and the degree of tumor tissue infiltration and is known to influence treatment efficacies. As a result, the idea of an immunoscore, identifying a patient's immunophenotype, emerged (*61*). Our work uncovered several immunophenotypes within expanded TILs from OvCa patients by multicolor flow cytometry compared to previous immunohistochemistry based analysis (*62*). As described by Sato *et al*. (2005) (*37*) and Zhang *et al*. (2003) (*38*) high numbers of intraepithelial $CD8^+$ TILs are associated with better prognosis in OvCa. We found that OvCa TILs were largely composed of $CD4^+$ rather than $CD8^+$ TILs. In this regard, OvCa models with high amounts of suppressive $CD4^+$ TILs and low numbers of $CD8^+$ TILs are suggested to have worse prognosis (*63*). In line with previous reports (*64*), we identified expression of CD39 in OvCa TIL populations, a marker that distinguishes between tumor-specific CTLs ($CD39^+$) and bystander TILs ($CD39^-$) (*41, 42*). Interestingly, we found that $CD8^+$ TIL amounts correlated with that of $CD8^+$ $CD39^+$ TILs, and could confirm that these tumor-specific T cells constitute an exhausted, memory T cell like phenotype, as CD39 expression was limited to $CD8^+PD\text{-}1^+$ TILs. Importantly, our results further demonstrated that co-cultures of PDM and autologous TILs could be applied to assess the treatment effect of CPIs in a preclinical and patient-specific setting. Such PDM-TIL co-culture systems could potentially be used to identify OvCa patients, who would most likely benefit from immunotherapies. According to the data presented here, OvCa tumors with regional lymph node metastasis contained higher numbers of $CD8^+$ and $CD8^+CD39^+$ TILs. The co-culture models tested in our study for response towards CPI treatment were derived from lymph-node spreading primary tumors, which might suggest that immunogenicity of OvCa increases upon metastasis.

Limitations of our PDM model are currently the restricted number of PDM available from digestion of individual tumor tissue samples. From experience with different tumor types, an average of several hundred to several thousand microtumors can be isolated from fresh tissue samples. This number depends on the amount of tissue available for PDM isolation as well as tissue composition (including degree of fibrosis and necrosis). PDMs are therefore presently not suitable for high-throughput drug screening approaches, but for focused drug testing in late preclinical and translational drug development as well as in the context of precision oncology. Since PDM generally show a low proliferation rate in culture, passaging and propagation of these models is currently not feasible; at the same time, it should be considered that dissociation during passaging of PDM would probably dissolve their valuable tissue-like structure and would be accordingly disadvantageous. Similar to patient-derived tumor organoids, PDM can be cryopreserved and thus applied in repetitive analyses.
In addition to new methods of molecular tumor analysis and diagnostics, patient-derived model systems including the one we introduce here are expected to play an important role in personalized oncology in order to identify suitable and effective therapies for the individual patient as well as existing therapeutic resistances of the patient's tumor.

Materials and Methods

Human specimens

Ovarian tumor samples were obtained from nineteen patients diagnosed with ovarian cancer undergoing surgery at the Center for Women's Health, University Hospital Tuebingen. Written informed consent was obtained from all participants. The tumors were classified according to International Federation of Gynecology and Obstetrics (FIGO) grading system. Tumor samples were delivered on the day of operation. The research project was approved by the ethics committee (IRB#275/2017BO2 and IRB#788/2018BO2).

Isolation and cultivation of patient-derived microtumors and tumor-infiltrating Lymphocytes

The procedure was adapted from Kondo et al. (2011) (*11*) and modified as follows. Tumor specimens were washed in HBSS (Gibco), minced with forceps, and digested with LiberaseTM DH (*65*) for 2h at 37°C. Digested tissue was centrifuged (300g, 5 min), washed with HBSS and filtered through a stainless 500 µm steel mesh (VWR). The flow-through was again filtered through a 40 µm cell strainer (Corning). The filtrate containing the TIL fraction was resuspended in Advanced RPMI 1640 (Gibco) supplemented with 2 mM Glutamine (Gibco), 1% MEM Vitamins (Gibco), 5% human serum (Sigma-Aldrich) and 100 µg/ml primocin (Invivogen). IL-2 (100 U/ml), IL-7 (10 U/ml) and IL-15 (23.8 U/ml) (Peprotech) were freshly added to culture media. For expansion, CD3/CD28 dynabeads were added (Milteny Biotech). PDM, held back by cell strainer, were washed in HBSS and cultured in suspension in StemPro® hESC SFM (Gibco) supplemented with 8 ng/ml FGF-basic (Gibco), 0.1 mM β-mercaptoethanol (Gibco), 1.8% BSA (Gibco) and 100 µg/ml primocin (Invivogen) within cell-repellent culture dish (60x15 mm) (Corning).

RPPA and protein data analysis

Detailed methods of sample preparation and RPPA processing are provided in SI Materials. RPPA protein analysis and protein data processing was applied as reported before (*66-68*). Detailed methods of sample preparation and RPPA processing are provided in SI Materials. From the arrays, PDM sample signals were extracted as protein-normalized, background-corrected mean fluorescence intensity (NFI), as measured from two technical sample replicates. NFI signals, median-centered for each protein over all measured samples (including OvCa PDM and BC PDM samples) and log2 transformed, reflect a measure for relative protein abundance. Small

NFI protein signals at around blank assay level (0.02 NFI) were as a limiting quality criterion excluded from further analysis; otherwise all NFI signals were used for further protein data analysis. Protein heat maps were generated and cluster analysis (HCL) performed using the freely available MultiExperiment Viewer (MeV) software. For the comparison of protein profiles of treatment responders and non-responders (defined by functional compound testing; Fig. 3C, Fig. S2), only proteins with a >20% difference between the means were used for analysis. On- and off-target pathway effects were evaluated from one biological and two technical replicate samples per model at three different treatment times (0.5, 4 and 72 h). Treated sample to respective DMSO vehicle control NFI ratios (TR) were calculated for each treatment condition and log2-transformed. If possible, the protein abundances were shown as mean of responder/non-responder or both (analyzed beforehand by functional compound testing; Fig. 2C). A treatment-specific threshold of protein change (carboplatin: minimum 50% difference; selumetinib: minimum 100% difference) was set. Only proteins showing treatment effects above the threshold were shown.

Efficacy of compounds validated in PDM cultures

Efficacy of compounds was validated by applying the real-time CellTox™ Green Cytotoxicity assay (Promega). Assays were performed according to manufacturer's protocol. PDM were cultured a maximum of 1-2 weeks in PDM culture medium prior testing. Per treatment three to eight replicates were performed using n = 15 PDM per replicate in a total volume of 150 µl phenol-red free PDM culture medium. Cell death was measured as relative fluorescent unit (RFU) (485–500 nm Ex / 520–530 nm Em), relative to the number of dead, permeable cells after 24h, 48h and 72h with the Envision Multilabel Plate Reader 2102 and Tecan Spark Multimode Plate Reader. RFU values were normalized to DMSO control or H_2O control according to used drug solvent. Treatment effects were measured as fold change (FC) compared to control. Differences between treated PDM and untreated PDM were calculated as fold change values separately for each time point. Statistical significance was evaluated by two-way ANOVA multiple comparison test. Outliers were identified with the Iglewicz and Hoaglin's robust test for multiple outliers applying a recommended Z-score of ≥ 3.5 (*69*).

Statistical analysis

Statistical analysis was performed using GraphPad Prism. For Boxplot data, whiskers represent quartiles with minimum and maximum values and the median. Datasets with no clear normal distribution were analyzed with unpaired, two-tailed Mann-Whitney-U-test, otherwise as indicated. Correlation data were evaluated by Spearmans rank correlation. For all analyses, P values < 0.05 were considered statistically significant. Recommended post-hoc tests were applied for multiple comparisons.

References

1. F. Bray, J. Ferlay, I. Soerjomataram, R. L. Siegel, L. A. Torre, A. Jemal, Global cancer statistics 2018: GLOBOCAN estimates of incidence and mortality worldwide for 36 cancers in 185 countries. *CA Cancer J. Clin.* **68**, 394-424 (2018).
2. B. Izar, I. Tirosh, E. H. Stover, I. Wakiro, M. S. Cuoco, I. Alter, C. Rodman, R. Leeson, M. J. Su, P. Shah, M. Iwanicki, S. R. Walker, A. Kanodia, J. C. Melms, S. Mei, J. R. Lin, C. B. M. Porter, M. Slyper, J. Waldman, L. Jerby-Arnon, O. Ashenberg, T. J. Brinker, C. Mills, M. Rogava, S. Vigneau, P. K. Sorger, L. A. Garraway, P. A. Konstantinopoulos, J. F. Liu, U. Matulonis, B. E. Johnson, O. Rozenblatt-Rosen, A. Rotem, A. Regev, A single-cell landscape of high-grade serous ovarian cancer. *Nat. Med.* **26**, 1271-1279 (2020).
3. T. C. G. A. R. Network, Integrated genomic analyses of ovarian carcinoma. *Nature* **474**, 609-615 (2011).
4. H. Zhang, T. Liu, Z. Zhang, S. H. Payne, B. Zhang, J. E. McDermott, J.-Y. Zhou, V. A. Petyuk, L. Chen, D. Ray, S. Sun, F. Yang, L. Chen, J. Wang, P. Shah, S. W. Cha, P. Aiyetan, S. Woo, Y. Tian, M. A. Gritsenko, T. R. Clauss, C. Choi, M. E. Monroe, S. Thomas, S. Nie, C. Wu, R. J. Moore, K.-H. Yu, D. L. Tabb, D. Fenyö, V. Bafna, Y. Wang, H. Rodriguez, E. S. Boja, T. Hiltke, R. C. Rivers, L. Sokoll, H. Zhu, I.-M. Shih, L. Cope, A. Pandey, B. Zhang, M. P. Snyder, D. A. Levine, R. D. Smith, D. W. Chan, K. D. Rodland, S. A. Carr, M. A. Gillette, K. R. Klauser, E. Kuhn, D. R. Mani, P. Mertins, K. A. Ketchum, R. Thangudu, S. Cai, M. Oberti, A. G. Paulovich, J. R. Whiteaker, N. J. Edwards, P. B. McGarvey, S. Madhavan, P. Wang, D. W. Chan, A. Pandey, I.-M. Shih, H. Zhang, Z. Zhang, H. Zhu, L. Cope, G. A. Whiteley, S. J. Skates, F. M. White, D. A. Levine, E. S. Boja, C. R. Kinsinger, T. Hiltke, M. Mesri, R. C. Rivers, H. Rodriguez, K. M. Shaw, S. E. Stein, D. Fenyo, T. Liu, J. E. McDermott, S. H. Payne, K. D. Rodland, R. D. Smith, P. Rudnick, M. Snyder, Y. Zhao, X. Chen, D. F. Ransohoff, A. N. Hoofnagle, D. C. Liebler, M. E. Sanders, Z. Shi, R. J. C. Slebos, D. L. Tabb, B. Zhang, L. J. Zimmerman, Y. Wang, S. R. Davies, L. Ding, M. J. C. Ellis, R. R. Townsend, Integrated Proteogenomic Characterization of Human High-Grade Serous Ovarian Cancer. *Cell* **166**, 755-765 (2016).
5. M. Verduin, A. Hoeben, D. De Ruysscher, M. Vooijs, Patient-Derived Cancer Organoids as Predictors of Treatment Response. *Front. Oncol.* **11**, 641980 (2021).
6. H. Chen, K. Gotimer, C. De Souza, C. G. Tepper, A. N. Karnezis, G. S. Leiserowitz, J. Chien, L. H. Smith, Short-term organoid culture for drug sensitivity testing of high-grade serous carcinoma. *Gynecol. Oncol.* **157**, 783-792 (2020).
7. O. Kopper, C. J. De Witte, K. Lõhmussaar, J. E. Valle-Inclan, N. Hami, L. Kester, A. V. Balgobind, J. Korving, N. Proost, H. Begthel, L. M. Van Wijk, S. A. Revilla, R. Theeuwsen, M. Van De Ven, M. J. Van Roosmalen, B. Ponsioen, V. W. H. Ho, B. G. Neel, T. Bosse, K. N. Gaarenstroom, H. Vrieling, M. P. G. Vreeswijk, P. J. Van Diest, P. O. Witteveen, T. Jonges, J. L. Bos, A. Van Oudenaarden, R. P. Zweemer, H. J. G. Snippert, W. P. Kloosterman, H. Clevers, An organoid platform for ovarian cancer captures intra- and interpatient heterogeneity. *Nat. Med.* **25**, 838-849 (2019).
8. S. J. Hill, B. Decker, E. A. Roberts, N. S. Horowitz, M. G. Muto, M. J. Worley, Jr., C. M. Feltmate, M. R. Nucci, E. M. Swisher, H. Nguyen, C. Yang, R. Morizane, B. S. Kochupurakkal, K. T. Do, P. A. Konstantinopoulos, J. F. Liu, J. V. Bonventre, U. A. Matulonis, G. I. Shapiro, R. S. Berkowitz, C. P. Crum, A. D. D'Andrea, Prediction of DNA

Repair Inhibitor Response in Short-Term Patient-Derived Ovarian Cancer Organoids. *Cancer Discov.* **8**, 1404-1421 (2018).
9. J. T. Neal, X. Li, J. Zhu, V. Giangarra, C. L. Grzeskowiak, J. Ju, I. H. Liu, S.-H. Chiou, A. A. Salahudeen, A. R. Smith, B. C. Deutsch, L. Liao, A. J. Zemek, F. Zhao, K. Karlsson, L. M. Schultz, T. J. Metzner, L. D. Nadauld, Y.-Y. Tseng, S. Alkhairy, C. Oh, P. Keskula, D. Mendoza-Villanueva, F. M. De La Vega, P. L. Kunz, J. C. Liao, J. T. Leppert, J. B. Sunwoo, C. Sabatti, J. S. Boehm, W. C. Hahn, G. X. Y. Zheng, M. M. Davis, C. J. Kuo, Organoid Modeling of the Tumor Immune Microenvironment. *Cell* **175**, 1972-1988.e1916 (2018).
10. G. E. Wensink, S. G. Elias, J. Mullenders, M. Koopman, S. F. Boj, O. W. Kranenburg, J. M. L. Roodhart, Patient-derived organoids as a predictive biomarker for treatment response in cancer patients. *npj Precision Oncology* **5**, (2021).
11. J. Kondo, H. Endo, H. Okuyama, O. Ishikawa, H. Iishi, M. Tsujii, M. Ohue, M. Inoue, Retaining cell-cell contact enables preparation and culture of spheroids composed of pure primary cancer cells from colorectal cancer. *Proc. Natl. Acad. Sci. U. S. A.* **108**, 6235-6240 (2011).
12. M. Köbel, K. Rahimi, P. F. Rambau, C. Naugler, C. Le Page, L. Meunier, M. De Ladurantaye, S. Lee, S. Leung, E. L. Goode, S. J. Ramus, J. W. Carlson, X. Li, C. A. Ewanowich, L. E. Kelemen, B. Vanderhyden, D. Provencher, D. Huntsman, C.-H. Lee, C. B. Gilks, A.-M. Mes Masson, An Immunohistochemical Algorithm for Ovarian Carcinoma Typing. *Int. J. Gynecol. Pathol.* **35**, 430-441 (2016).
13. T. Hilliard, The Impact of Mesothelin in the Ovarian Cancer Tumor Microenvironment. *Cancers (Basel)* **10**, 277 (2018).
14. R. Hassan, R. J. Kreitman, I. Pastan, M. C. Willingham, Localization of Mesothelin in Epithelial Ovarian Cancer. *Appl. Immunohistochem. Mol. Morphol.* **13**, 243-247 (2005).
15. M.-C. Chang, C.-A. Chen, P.-J. Chen, Y.-C. Chiang, Y.-L. Chen, T.-L. Mao, H.-W. Lin, W.-H. Lin Chiang, W.-F. Cheng, Mesothelin enhances invasion of ovarian cancer by inducing MMP-7 through MAPK/ERK and JNK pathways. *Biochem. J.* **442**, 293-302 (2012).
16. C. Tornos, R. Soslow, S. Chen, M. Akram, A. J. Hummer, N. Abu-Rustum, L. Norton, L. K. Tan, Expression of WT1, CA 125, and GCDFP-15 as useful markers in the differential diagnosis of primary ovarian carcinomas versus metastatic breast cancer to the ovary. *Am. J. Surg. Pathol.* **29**, 1482-1489 (2005).
17. D. Kriplani, M. M. Patel, Immunohistochemistry: A diagnostic aid in differentiating primary epithelial ovarian tumors and tumors metastatic to the ovary. *South Asian Journal of Cancer* **02**, 254-258 (2013).
18. W. Neunteufel, G. Breitenecker, Tissue expression of CA 125 in benign and malignant lesions of ovary and fallopian tube: a comparison with CA 19-9 and CEA. *Gynecol. Oncol.* **32**, 297-302 (1989).
19. T. R. Cox, The matrix in cancer. *Nature Reviews Cancer* **21**, 217-238 (2021).
20. R. Bhat, M. J. Bissell, Of plasticity and specificity: dialectics of the microenvironment and macroenvironment and the organ phenotype. *WIREs Developmental Biology* **3**, 147-163 (2014).
21. C. D. Roskelley, M. J. Bissell, The dominance of the microenvironment in breast and ovarian cancer. *Semin. Cancer Biol.* **12**, 97-104 (2002).
22. P. Mhawech-Fauceglia, L. Yan, M. Sharifian, X. Ren, S. Liu, G. Kim, S. A. Gayther, T. Pejovic, K. Lawrenson, Stromal Expression of Fibroblast Activation Protein Alpha (FAP)

Predicts Platinum Resistance and Shorter Recurrence in patients with Epithelial Ovarian Cancer. *Cancer Microenviron.* **8**, 23-31 (2015).
23. N. I. Nissen, M. Karsdal, N. Willumsen, Collagens and Cancer associated fibroblasts in the reactive stroma and its relation to Cancer biology. *J. Exp. Clin. Cancer Res.* **38**, 115 (2019).
24. P. Saha, K. Datta, Multi-functional, multicompartmental hyaluronan-binding protein 1 (HABP1/p32/gC1qR): implication in cancer progression and metastasis. *Oncotarget* **9**, 10784-10807 (2018).
25. M. Longacre, N. Snyder, G. Housman, M. Leary, K. Lapinska, S. Heerboth, A. Willbanks, S. Sarkar, A Comparative Analysis of Genetic and Epigenetic Events of Breast and Ovarian Cancer Related to Tumorigenesis. *Int. J. Mol. Sci.* **17**, 759 (2016).
26. M. Iyengar, P. O'Hayer, A. Cole, T. Sebastian, K. Yang, L. Coffman, R. J. Buckanovich, CDK4/6 inhibition as maintenance and combination therapy for high grade serous ovarian cancer. *Oncotarget* **9**, 15658-15672 (2018).
27. J. Farley, W. E. Brady, V. Vathipadiekal, H. A. Lankes, R. Coleman, M. A. Morgan, R. Mannel, S. D. Yamada, D. Mutch, W. H. Rodgers, M. Birrer, D. M. Gershenson, Selumetinib in women with recurrent low-grade serous carcinoma of the ovary or peritoneum: an open-label, single-arm, phase 2 study. *The Lancet Oncology* **14**, 134-140 (2013).
28. N. McGivern, A. El-Helali, P. Mullan, I. A. McNeish, D. Paul Harkin, R. D. Kennedy, N. McCabe, Activation of MAPK signalling results in resistance to saracatinib (AZD0530) in ovarian cancer. *Oncotarget* **9**, 4722-4736 (2018).
29. D. R. Liston, M. Davis, Clinically Relevant Concentrations of Anticancer Drugs: A Guide for Nonclinical Studies. *Clin. Cancer. Res.* **23**, 3489-3498 (2017).
30. S. Ovejero, A. Bueno, M. P. Sacristán, Working on Genomic Stability: From the S-Phase to Mitosis. *Genes* **11**, 225 (2020).
31. J. Holder, E. Poser, F. A. Barr, Getting out of mitosis: spatial and temporal control of mitotic exit and cytokinesis byPP1 andPP2A. *FEBS Lett.* **593**, 2908-2924 (2019).
32. J. Aramburu, M. C. Ortells, S. Tejedor, M. Buxadé, C. López-Rodríguez, Transcriptional regulation of the stress response by mTOR. *Science Signaling* **7**, re2 (2014).
33. J. R. Dry, S. Pavey, C. A. Pratilas, C. Harbron, S. Runswick, D. Hodgson, C. Chresta, R. McCormack, N. Byrne, M. Cockerill, A. Graham, G. Beran, A. Cassidy, C. Haggerty, H. Brown, G. Ellison, J. Dering, B. S. Taylor, M. Stark, V. Bonazzi, S. Ravishankar, L. Packer, F. Xing, D. B. Solit, R. S. Finn, N. Rosen, N. K. Hayward, T. French, P. D. Smith, Transcriptional Pathway Signatures Predict MEK Addiction and Response to Selumetinib (AZD6244). *Cancer Res.* **70**, 2264-2273 (2010).
34. M. L. Fernandez, A. Dawson, J. Hoenisch, H. Kim, S. Bamford, C. Salamanca, G. DiMattia, T. Shepherd, M. Cremona, B. Hennessy, S. Anderson, S. Volik, C. C. Collins, D. G. Huntsman, M. S. Carey, Markers of MEK inhibitor resistance in low-grade serous ovarian cancer: EGFR is a potential therapeutic target. *Cancer Cell Int.* **19**, 10 (2019).
35. J. Megyesi, A. Tarcsafalvi, N. Seng, R. Hodeify, P. Price, Cdk2 phosphorylation of Bcl-xL after stress converts it to a pro-apoptotic protein mimicking Bax/Bak. *Cell Death Discovery* **2**, 15066 (2016).
36. E. B. Garon, R. S. Finn, W. Hosmer, J. Dering, C. Ginther, S. Adhami, N. Kamranpour, S. Pitts, A. Desai, D. Elashoff, T. French, P. Smith, D. J. Slamon, Identification of Common Predictive Markers of In vitro Response to the Mek Inhibitor Selumetinib (AZD6244;

ARRY-142886) in Human Breast Cancer and Non-Small Cell Lung Cancer Cell Lines. *Mol. Cancer Ther.* **9**, 1985-1994 (2010).
37. E. Sato, S. H. Olson, J. Ahn, B. Bundy, H. Nishikawa, F. Qian, A. A. Jungbluth, D. Frosina, S. Gnjatic, C. Ambrosone, J. Kepner, T. Odunsi, G. Ritter, S. Lele, Y. T. Chen, H. Ohtani, L. J. Old, K. Odunsi, Intraepithelial CD8+ tumor-infiltrating lymphocytes and a high CD8+/regulatory T cell ratio are associated with favorable prognosis in ovarian cancer. *Proc. Natl. Acad. Sci. U. S. A.* **102**, 18538-18543 (2005).
38. L. Zhang, J. R. Conejo-Garcia, D. Katsaros, P. A. Gimotty, M. Massobrio, G. Regnani, A. Makrigiannakis, H. Gray, K. Schlienger, M. N. Liebman, S. C. Rubin, G. Coukos, Intratumoral T Cells, Recurrence, and Survival in Epithelial Ovarian Cancer. *New Engl. J. Med.* **348**, 203-213 (2003).
39. J. Hamanishi, M. Mandai, M. Iwasaki, T. Okazaki, Y. Tanaka, K. Yamaguchi, T. Higuchi, H. Yagi, K. Takakura, N. Minato, T. Honjo, S. Fujii, Programmed cell death 1 ligand 1 and tumor-infiltrating CD8+ T lymphocytes are prognostic factors of human ovarian cancer. *Proceedings of the National Academy of Sciences* **104**, 3360-3365 (2007).
40. Q. Ye, D. G. Song, M. Poussin, T. Yamamoto, A. Best, C. Li, G. Coukos, D. J. Powell, CD137 Accurately Identifies and Enriches for Naturally Occurring Tumor-Reactive T Cells in Tumor. *Clin. Cancer. Res.* **20**, 44-55 (2014).
41. T. Duhen, R. Duhen, R. Montler, J. Moses, T. Moudgil, N. F. de Miranda, C. P. Goodall, T. C. Blair, B. A. Fox, J. E. McDermott, S. C. Chang, G. Grunkemeier, R. Leidner, R. B. Bell, A. D. Weinberg, Co-expression of CD39 and CD103 identifies tumor-reactive CD8 T cells in human solid tumors. *Nat Commun* **9**, 2724 (2018).
42. Y. Simoni, E. Becht, M. Fehlings, C. Y. Loh, S.-L. Koo, K. W. W. Teng, J. P. S. Yeong, R. Nahar, T. Zhang, H. Kared, K. Duan, N. Ang, M. Poidinger, Y. Y. Lee, A. Larbi, A. J. Khng, E. Tan, C. Fu, R. Mathew, M. Teo, W. T. Lim, C. K. Toh, B.-H. Ong, T. Koh, A. M. Hillmer, A. Takano, T. K. H. Lim, E. H. Tan, W. Zhai, D. S. W. Tan, I. B. Tan, E. W. Newell, Bystander CD8+ T cells are abundant and phenotypically distinct in human tumour infiltrates. *Nature* **557**, 575-579 (2018).
43. F. P. Canale, M. C. Ramello, N. Núñez, C. L. A. Furlan, S. N. Bossio, M. G. Serrán, J. T. Boari, A. Del Castillo, M. Ledesma, C. Sedlik, E. Piaggio, A. Gruppi, E. V. A. Rodríguez, C. L. Montes, CD39 Expression Defines Cell Exhaustion in Tumor-Infiltrating CD8+T Cells. *Cancer Res.* **78**, 115-128 (2018).
44. C. S. Jansen, N. Prokhnevska, V. A. Master, M. G. Sanda, J. W. Carlisle, M. A. Bilen, M. Cardenas, S. Wilkinson, R. Lake, A. G. Sowalsky, R. M. Valanparambil, W. H. Hudson, D. McGuire, K. Melnick, A. I. Khan, K. Kim, Y. M. Chang, A. Kim, C. P. Filson, M. Alemozaffar, A. O. Osunkoya, P. Mullane, C. Ellis, R. Akondy, S. J. Im, A. O. Kamphorst, A. Reyes, Y. Liu, H. Kissick, An intra-tumoral niche maintains and differentiates stem-like CD8 T cells. *Nature* **576**, 465-470 (2019).
45. J. M. Przystal, H. Becker, D. Canjuga, F. Tsiami, N. Anderle, A.-L. Keller, A. Pohl, C. H. Ries, M. Schmittnaegel, N. Korinetska, M. Koch, J. Schittenhelm, M. Tatagiba, C. Schmees, S. C. Beck, G. Tabatabai, Targeting CSF1R Alone or in Combination with PD1 in Experimental Glioma. *Cancers (Basel)* **13**, 2400 (2021).
46. B. Walter, D. Canjuga, S. G. Yüz, M. Ghosh, P. Bozko, J. M. Przystal, P. Govindarajan, N. Anderle, A. L. Keller, M. Tatagiba, K. Schenke-Layland, H. G. Rammensee, S. Stevanovic, N. P. Malek, C. Schmees, G. Tabatabai, Argyrin F Treatment-Induced Vulnerabilities Lead

to a Novel Combination Therapy in Experimental Glioma. *Advanced Therapeutics*, 2100078 (2021).
47. G. Yu, J. Wang, Significance of hyaluronan binding protein (HABP1/P32/gC1qR) expression in advanced serous ovarian cancer patients. **94**, 210-215 (2013).
48. H. Yu, Q. Liu, T. Xin, L. Xing, G. Dong, Q. Jiang, Y. Lv, X. Song, C. Teng, D. Huang, Y. Li, W. Shen, C. Teng, Y. Jin, F. Zhang, Elevated expression of hyaluronic acid binding protein 1 (HABP1)/P32/C1QBP is a novel indicator for lymph node and peritoneal metastasis of epithelial ovarian cancer patients. *Tumor Biol.* **34**, 3981-3987 (2013).
49. B. Barnett, I. Kryczek, P. Cheng, W. Zou, T. J. Curiel, Regulatory T cells in ovarian cancer: biology and therapeutic potential. *Am. J. Reprod. Immunol.* **54**, 369-377 (2005).
50. F. Valeriote, L. van Putten, Proliferation-dependent cytotoxicity of anticancer agents: a review. *Cancer Res.* **35**, 2619-2630 (1975).
51. P. A. Vasey, Resistance to chemotherapy in advanced ovarian cancer: mechanisms and current strategies. *Br. J. Cancer* **89**, 23-28 (2003).
52. C. L. W. Haygood, Ovarian cancer stem cells: Can targeted therapy lead to improved progression-free survival? *World Journal of Stem Cells* **6**, 441 (2014).
53. S. A. Bapat, A. M. Mali, C. B. Koppikar, N. K. Kurrey, Stem and Progenitor-Like Cells Contribute to the Aggressive Behavior of Human Epithelial Ovarian Cancer. *Cancer Res.* **65**, 3025-3029 (2005).
54. J. Deng, L. Wang, H. Chen, J. Hao, J. Ni, L. Chang, W. Duan, P. Graham, Y. Li, Targeting epithelial-mesenchymal transition and cancer stem cells for chemoresistant ovarian cancer. *Oncotarget* **7**, 55771-55788 (2016).
55. S. Liu, J. Sun, B. Cai, X. Xi, L. Yang, Z. Zhang, Y. Feng, Y. Sun, NANOG regulates epithelial-mesenchymal transition and chemoresistance through activation of the STAT3 pathway in epithelial ovarian cancer. *Tumor Biol.* **37**, 9671-9680 (2016).
56. K. Balmanno, S. D. Chell, A. S. Gillings, S. Hayat, S. J. Cook, Intrinsic resistance to the MEK1/2 inhibitor AZD6244 (ARRY-142886) is associated with weak ERK1/2 signalling and/or strong PI3K signalling in colorectal cancer cell lines. *Int. J. Cancer* **125**, 2332-2341 (2009).
57. C. H. Lee, K. Inoki, M. Karbowniczek, E. Petroulakis, N. Sonenberg, E. P. Henske, K. L. Guan, Constitutive mTOR activation in TSC mutants sensitizes cells to energy starvation and genomic damage via p53. *The EMBO journal* **26**, 4812-4823 (2007).
58. D. D. Vadysirisack, F. Baenke, B. Ory, K. Lei, L. W. Ellisen, Feedback control of p53 translation by REDD1 and mTORC1 limits the p53-dependent DNA damage response. *Mol. Cell. Biol.* **31**, 4356-4365 (2011).
59. O. V. Leontieva, M. V. Blagosklonny, DNA damaging agents and p53 do not cause senescence in quiescent cells, while consecutive re-activation of mTOR is associated with conversion to senescence. *Aging (Albany NY)* **2**, 924-935 (2010).
60. M. V. Astle, K. M. Hannan, P. Y. Ng, R. S. Lee, A. J. George, A. K. Hsu, Y. Haupt, R. D. Hannan, R. B. Pearson, AKT induces senescence in human cells via mTORC1 and p53 in the absence of DNA damage: implications for targeting mTOR during malignancy. *Oncogene* **31**, 1949-1962 (2012).
61. T. F. Gajewski, H. Schreiber, Y.-X. Fu, Innate and adaptive immune cells in the tumor microenvironment. *Nat. Immunol.* **14**, 1014-1022 (2013).

62. W. T. Hwang, S. F. Adams, E. Tahirovic, I. S. Hagemann, G. Coukos, Prognostic significance of tumor-infiltrating T cells in ovarian cancer: a meta-analysis. *Gynecol. Oncol.* **124**, 192-198 (2012).
63. T. J. Curiel, G. Coukos, L. Zou, X. Alvarez, P. Cheng, P. Mottram, M. Evdemon-Hogan, J. R. Conejo-Garcia, L. Zhang, M. Burow, Y. Zhu, S. Wei, I. Kryczek, B. Daniel, A. Gordon, L. Myers, A. Lackner, M. L. Disis, K. L. Knutson, L. Chen, W. Zou, Specific recruitment of regulatory T cells in ovarian carcinoma fosters immune privilege and predicts reduced survival. *Nat. Med.* **10**, 942-949 (2004).
64. G. Leem, J. Park, M. Jeon, E.-S. Kim, S. W. Kim, Y. J. Lee, S. J. Choi, B. Choi, S. Park, Y. S. Ju, I. Jung, S. Kim, E.-C. Shin, J. Y. Lee, S.-H. Park, 4-1BB co-stimulation further enhances anti-PD-1-mediated reinvigoration of exhausted CD39⁺ CD8 T cells from primary and metastatic sites of epithelial ovarian cancers. *Journal for ImmunoTherapy of Cancer* **8**, e001650 (2020).
65. S. Shuford, C. Wilhelm, M. Rayner, A. Elrod, M. Millard, C. Mattingly, A. Lotstein, A. M. Smith, Q. J. Guo, L. O'Donnell, J. Elder, L. Puls, S. J. Weroha, X. Hou, V. Zanfagnin, A. Nick, M. P. Stany, G. L. Maxwell, T. Conrads, A. K. Sood, D. Orr, L. M. Holmes, M. Gevaert, H. E. Crosswell, T. M. DesRochers, Prospective Validation of an Ex Vivo, Patient-Derived 3D Spheroid Model for Response Predictions in Newly Diagnosed Ovarian Cancer. *Sci. Rep.* **9**, 11153 (2019).
66. F. Pirnia, M. Pawlak, G. G. Thallinger, B. Gierke, M. F. Templin, A. Kappeler, D. C. Betticher, B. Gloor, M. M. Borner, Novel functional profiling approach combining reverse phase protein microarrays and human 3-D ex vivo tissue cultures: expression of apoptosis-related proteins in human colon cancer. *Proteomics* **9**, 3535-3548 (2009).
67. M. Pawlak, N. O. Carragher, Reverse Phase Protein Arrays elucidate mechanisms-of-action and phenotypic response in 2D and 3D models. *Drug Discovery Today: Technologies* **23**, 7-16 (2017).
68. G. M. Kresbach, M. Pawlak, High Precision RPPA: Concept, Features, and Application Performance of the Integrated Zeptosens Platform. *Adv. Exp. Med. Biol.* **1188**, 31-59 (2019).
69. B. Iglewicz, D. C. Hoaglin, *How to detect and handle outliers*. ASQC basic references in quality control (Milwaukee, Wis. : ASQC Quality Press, Milwaukee, Wis., 1993), pp. ix, 87 p.

Data and materials availability

All data needed to evaluate the conclusions of the paper are available in the main text or the supplementary materials of this publication. Materials and further data are available upon request after signature of an MTA from the corresponding authors.

Acknowledgments

We gratefully acknowledge the Department of Women's Health, Women's University Hospital, Tuebingen University Hospital for excellent support, helpful discussions and providing fresh tumor tissue biopsies and corresponding FFPE material. We thank all patients and healthy volunteers enrolled for giving their informed consent for secondary use of residual tissue, respectively. The use of human samples was approved by the local ethics commission at the Medical Faculty of Tuebingen under IRB#275/2017BO2 and IRB#788/2018BO2.

Funding

Ministry of Baden-Wuerttemberg for Economic Affairs, Labor and Tourism grant 3-4332.62-HSG/84

Author Contributions

Conceptualization: N.A, C.S, M.P, K.SL, S.Y.B, A.H,
Methodology: N.A, B.G, M.P, AL.K
Investigation: N.A, B.G, M.P, A.K, AL.K, A.S, S.Y.B,
Project administration: N.A, C.S, A.K
Supervision: C.S, A.K
Writing – original draft: N.A, C.S
Writing – review & editing: N.A, C.S, M.P, AL.K, K.SL, A.K, S.Y.B, A.H, A.S

Competing Interest Statement

Andreas Hartkopf received consulting and speaking fees from GSK, AstraZeneca and Clovis. Nicole Anderle, André Koch, Berthold Gierke, Anna-Lena Keller, Annette Staebler, Sara Y. Brucker, Michael Pawlak, Katja Schenke-Layland and Christian Schmees declare no competing interests.

Figures and Tables

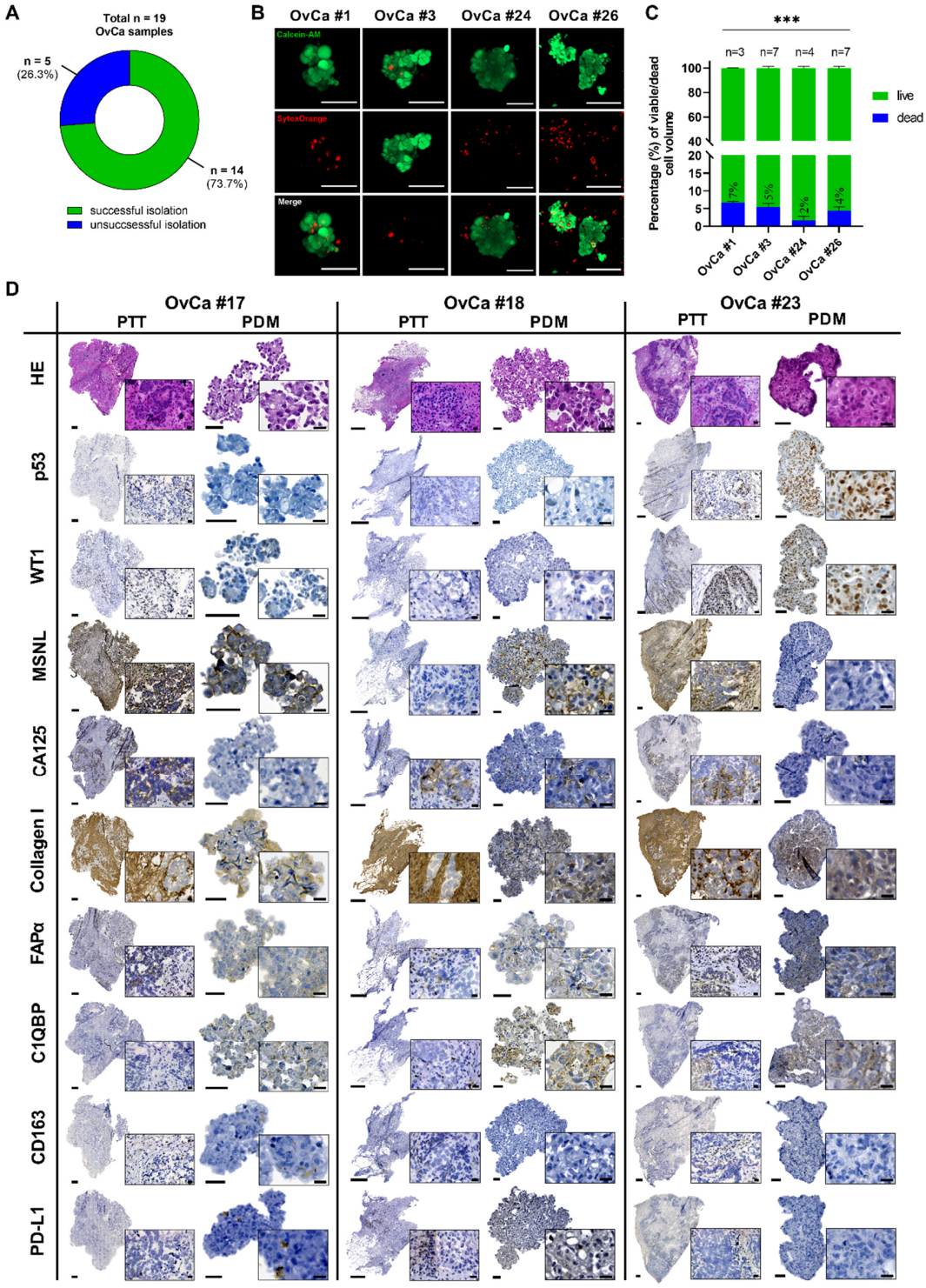

Figure 1. Patient-derived 3D microtumors (PDM) derived from primary OvCa tumor specimen show high viability and resemble histopathologocial features of the corresponding PTT. (**A**) Efficiency of isolating OvCa PDM from a total of n = 19 fresh primary OvCa tumor tissues samples. PDM gained from n = 14 specimen with a success rate of 73.7%. (**B**) Viability of OvCa PDM models. Exemplary 2D images from 3D projections of n = 4 OvCa PDM models confirm high viability according to Calcein-AM (viable cells) and SYTOX™ Orange (dead cells) staining. (**C**) Percentage of viable and dead cells in OvCa PDM. Viability was assessed by an image-based analysis (see SI Methods) in n = 4 OvCa PDM models shown in (B). Data are shown as mean values with SEM from at least n = 3 PDM of each model. *P < 0.05, **P < 0.01, ***P < 0.001, multiple paired t-test with Holm-Šídák's post hoc test. Scale bar 50 µm. (**D**) Hematoxylin and Eosin (H&E) as well as immunohistochemical staining of OvCa PDM and corresponding primary tumor tissue (PTT) sections. H&E stainings revealed features of malignant cells (incl. giant cells with more than one nucleolus, hyperchromatic cells and high nuclei:cytoplasma ratio) confirming the cancerous origin. Scale bars indicate 500 µm for PTT; 50 µm for PDM; 20 µm for magnifications (PTT and PDM). FAPα, cancer-associated fibroblast protein alpha; C1QBP, hyaluronan binding protein; WT1, wilms tumor 1; MSNL, mesothelin.

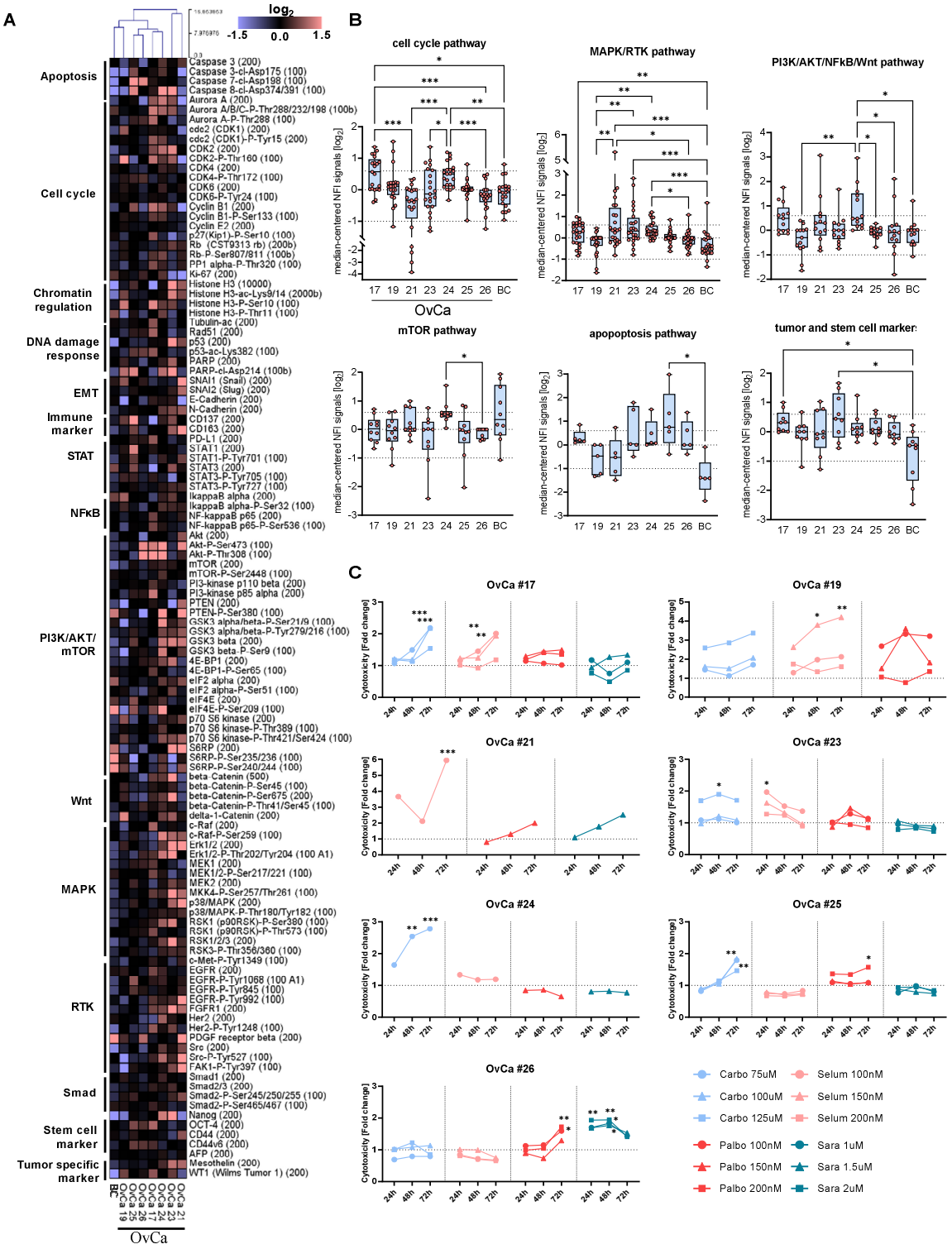
A
log2
-1.5
0.0
1.5
Apoptosis
Cell cycle
Chromatin regulation
DNA damage response
EMT
Immune marker
STAT
NFkB
PI3K/AKT/ mTOR
Wnt
MAPK
RTK
Smad
Stem cell marker
Tumor specific marker
OvCa
B
cell cycle pathway
MAPK/RTK pathway
PI3K/AKT/NFkB/Wnt pathway
mTOR pathway
apopoptosis pathway
tumor and stem cell marker
median-centered NFI signals [log2]
17 19 21 23 24 25 26 BC
OvCa
C
OvCa #17
OvCa #19
OvCa #21
OvCa #23
OvCa #24
OvCa #25
OvCa #26
Cytotoxicity [Fold change]
24h 48h 72h
Carbo 75uM
Carbo 100uM
Carbo 125uM
Selum 100nM
Selum 150nM
Selum 200nM
Palbo 100nM
Palbo 150nM
Palbo 200nM
Sara 1uM
Sara 1.5uM
Sara 2uM

Figure 2. RPPA protein profiling of OvCa PDM identifies significant differences in active protein signaling pathways as molecular basis for OvCa PDM drug treatment responses. (**A**) Protein heat map covering 116 analytes analyzed in OvCa PDM (n = 7) and BC PDM (n = 1) generated from sample sizes of n = 100-150 PDM. Protein abundances for each analyte are displayed as median-centered, log_2-transformed NFI signals. Samples were subjected to hierarchical clustering using Euclidean distance (complete linkage). (**B**) Activation state of different pathways in the different OvCa PDM models. Proteins related to an "active" pathway were selected for each of the plotted pathways (see Table S4). Protein signals are shown as median-centered, log_2 transformed NFI signals. Dotted lines indicate log_2 values of +0.6 (fold change of +1.5) and -1 log_2 (fold change of -0.5). Data are shown as box and whiskers plots with minimum and maximum range. *P < 0.05, **P < 0.01, ***P < 0.001, Kruskal-Wallis test with Dunn's post hoc test. (**C**) Cytotoxicity measurement of OvCa PDM treated with standard platinum-based chemotherapy (carbo 75-125 µM) and/or targeted therapy (selum 100-200 nM, palbo 100-200 nM, sara 1-2 µM). Four replicates per treatment with n = 15 PDM per well were performed and measured after 24 h, 48 h and 72 h. Signals were measured as RFU (Relative Fluorescent Unit), background corrected and normalized to vehicle control (DMSO). In case of palbociclib to H_2O control. Data are shown as mean values. Statistical significances compared to vehicle control or H_2O are shown. *P < 0.05, **P < 0.01, ***P < 0.001, Two-way ANOVA with Bonferroni's multiple comparison test. Carbo: carboplatin; Selum: selumetinib; Palbo: palbociclib; Sara: saracatenib

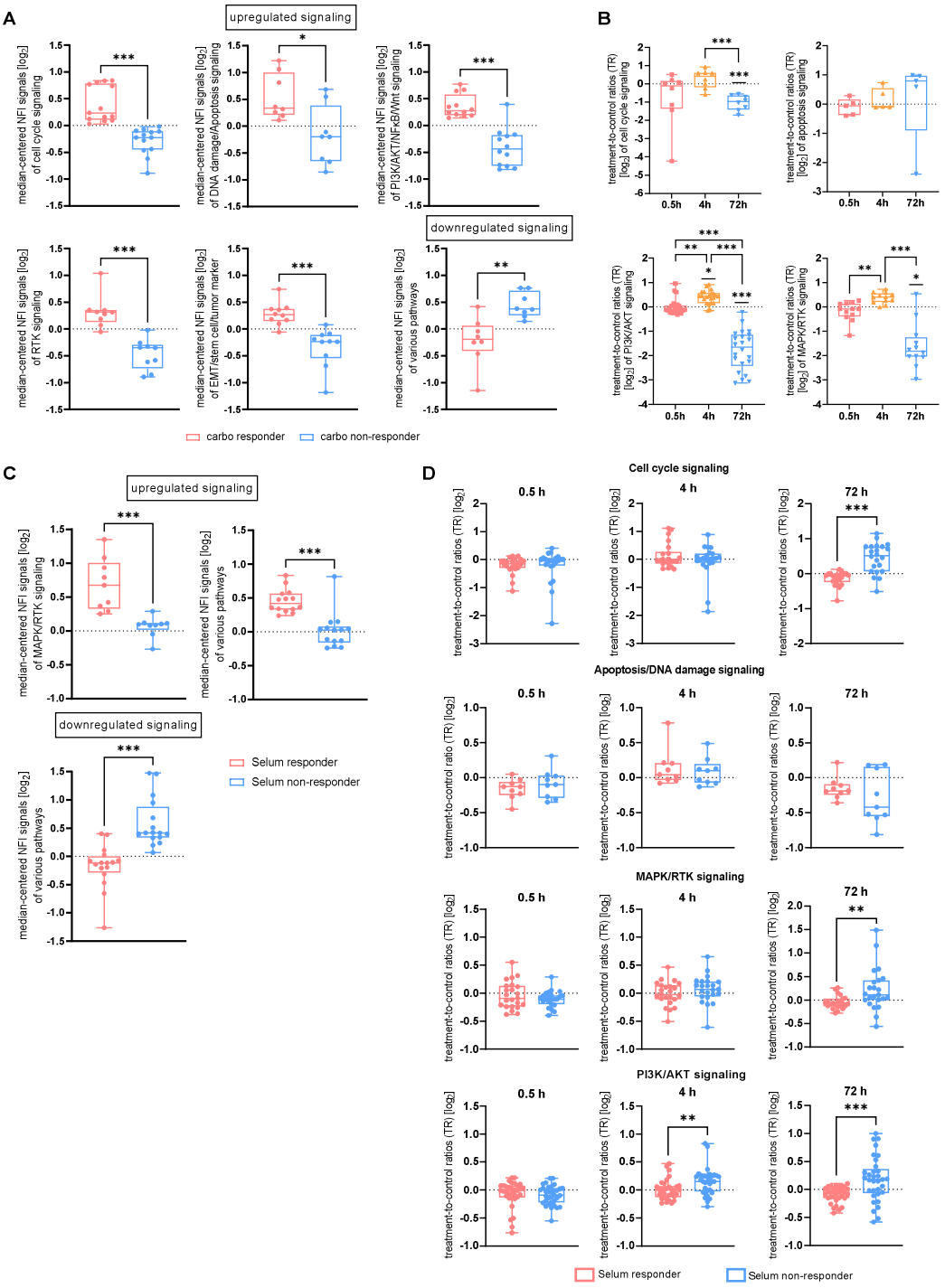

Figure 3. Carboplatin and selumetinib drug response in OvCa PDM correlates with the activity of diverse signaling pathways. (**A, C**) Signaling pathway activation in carboplatin (**A**) and selumetinib (**C**) responder vs. non-responder OvCa PDM. Proteins were sorted according to their pathway affiliation and according to upregulation or downregulation within responder group. **P* < 0.05, ***P* < 0.01, ****P* < 0.001, Mann-Whitney-U-test. R, responder; Non-R, Non-responder.

(**B**, **D**) Proteomic on- and off-target pathway effects in carboplatin- and selumetinib-treated OvCa PDM analyzed by RPPA. Treated PDM were analyzed from an immediate (0.5 h), an early (4 h) and a late (72 h) treatment time. For each time point, protein values are displayed as log_2-transformed treatment-to-control signal ratios (TR) calculated from NFI signals of treated PDM and corresponding vehicle control (DMSO). (**B**) OvCa #24 PDM were treated with 75 µM carboplatin. Only proteins with >50% differential protein abundance compared to vehicle control were selected, sorted according to pathway affiliation and plotted as box whisker plots. Significant differences between time points and vehicle control were measured. Straight lines above plots indicate statistical significances compared to vehicle control. *$P < 0.05$, **$P < 0.01$, ***$P < 0.001$, One-way ANOVA using nonparametric Kruskal-Wallis with Dunn's ad hoc test. (**D**) Proteomic on- and off-target pathway effects in selumetinib (100 nM) treated PDM. Selumetinib responder and non-responder PDM models were grouped. Only proteins with greater than 100% differential protein abundance between responder and non-responder PDM models were plotted according to signaling pathway affiliation. *$P < 0.05$, **$P < 0.01$, ***$P < 0.001$, Mann-Whitney U-test.

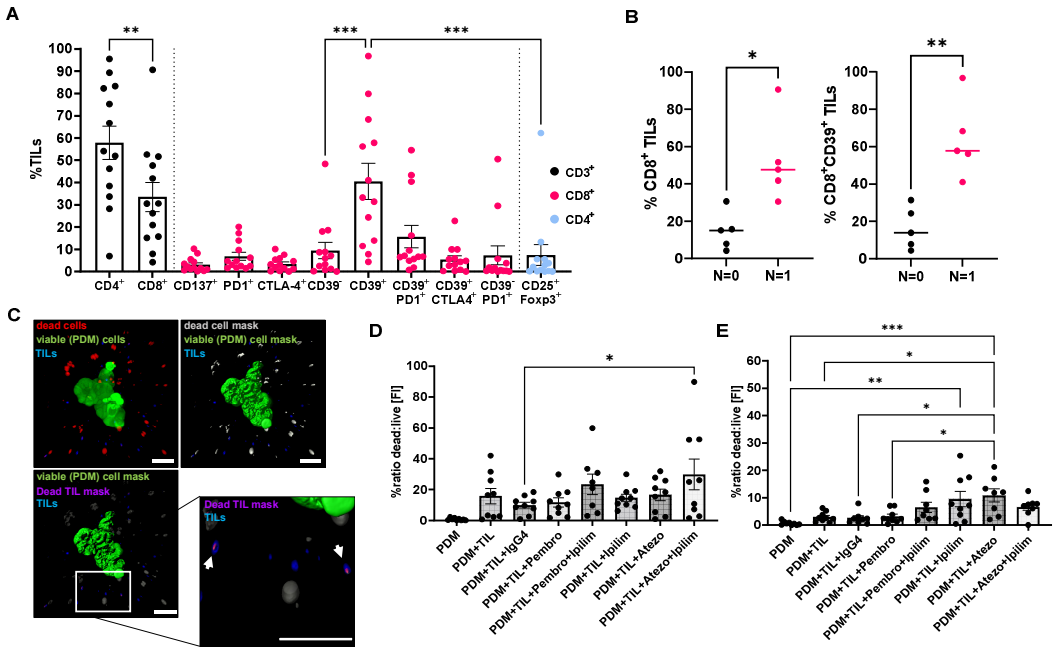

Figure 4. CPI treatment in OvCa PDM-TIL co-cultures increased functional TIL killing effects. Autologous TIL populations were isolated and expanded from OvCa tissue specimen. (**A**) Percentages of different TIL populations within CD3, CD8 and CD4 positive T cells of different models were quantified by multicolor flow cytometry. Data are shown as means ± SEM of at least n = 10 OvCa samples. *$P < 0.05$, **$P < 0.01$, ***$P < 0.001$, ANOVA with Holm-Šídák's post hoc test. (**B**) Percentages of $CD8^+$ and $CD8^+CD39^+$ TILs in OvCa patients with lymph node spread (N = 1) and without lymph node spread (N = 0). All points with median are shown. *$P < 0.05$, **$P < 0.01$, Mann-Whitney-U-test. (**C-E**) Killing effects of autologous TILs on corresponding PDM in co-cultures treated with immune checkpoint inhibitors (CPI). (**C**) PDM killing effects were measured in an image-based assay format as ratio of fluorescent intensities (FI) of dead cells vs. live PDM cells. Per treatment $n = 3$ PDM in three replicates were analyzed. Masks for viable PDM (Calcein-AM staining), dead cells (SYTOX™ Orange dead cell staining) and TILs (CellTracker™ Deep Red staining) were applied using Imaris 8.0 software. Scale bars indicate 50 µm. FI from TILs were subtracted from the total dead FI. TILs of OvCa #24 (**D**) and #26 (**E**) were co-cultured with $n = 15$ PDM using an E:T ratio of 4:1 and treated with CPI either alone or in combination. *$P < 0.05$, **$P < 0.01$, ***$P < 0.001$, ANOVA with Holm-Šídák's post hoc test. Pembro: pembrolizumab 60 µg/ml; Ipilim: ipilimumab 50 µg/ml; Atezo: atezolizumab 50 µg/ml.